Nanoscale

Accepted Manuscript

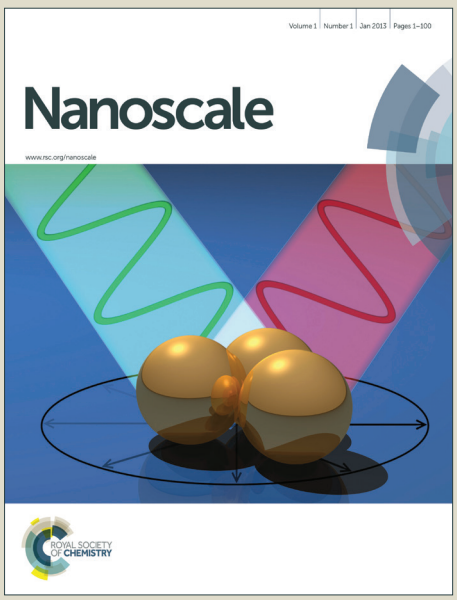

ROYAL SOCIETY OF CHEMISTRY

www.rsc.org/nanoscale

Cite this: DOI: 10.1039/c0xx00000x

www.rsc.org/xxxxxx

ARTICLE TYPE

Cu_3Si@Si core-shell nanoparticles synthesized by a solid-state reaction and their performance as anode materials for lithium ion batteries

Jianbin Zhou,[a] Ning Lin,[a] Ying Han,[a] Jie Zhou,[a] Yongchun Zhu,*[a] Jin Du[a] and Yitai Qian*[a]

Received (in XXX, XXX) Xth XXXXXXXXX 20XX, Accepted Xth XXXXXXXXX 20XX
DOI: 10.1039/b000000x

Cu_3Si@Si core-shell nanoparticles with Si shell coated over the Cu_3Si core are synthesized by a solid-state reaction between CuCl and Si. The evaluation process of the core-shell structure shows a mechanism analogous to Kirkendall effect. As anode materials for lithium ion batteries, Cu_3Si@Si core-shell nanoparticles retained a capacity of 903.6 mA h g^{-1} at the current density of 2 A g^{-1} over 400 cycles.

Recently, Si, as an anode material for rechargeable lithium-ion batteries (LIBs), has attracted increasing attention due to its high theoretical capacity of 3600 mA h g^{-1} and low electrochemical potential *vs.* Li/Li^+ (< 0.5 V).[1-4] However, the drawback in applying Si anode is the huge volume variation (> 300 %) during repeated lithiation/delithiation process and low intrinsic electrical conductivity, which can result in the pulverization of electrode and the rapid capacity fading upon cycling. [5-7]

One possible solution to overcome the drawbacks of Si is using core-shell Si based composite materials, in which electrochemically inactive matrix is added.[8,9] Since the inactive materials can alleviate the mechanical stresses experienced by the volume change of Si during the repeated discharge and charge process.[6] The coating of carbon, metal or metallic compound layer on the surface of Si materials is the typical way to fabricate core-shell materials.[10-13] Microporous carbon coated Si nanocomposites with core-shell structure were fabricated by in-situ polymerization followed by carbonization method. As anode materials, the synthesized Si@C core-shell nanocomposites exhibited a capacity of over 1200 mA h g^{-1} at 0.7 A g^{-1} after 40 cycles.[14] Si@SiO_2 core-shell nanocomposites were synthesized by a vesicle template method, which showed a capacity retention of 687 mA h g^{-1} at the current density of 0.05 A g^{-1} after 30 cycles.[15] Double-walled core-shell structure Si@SiO_2@C nanocomposites were prepared by calcination of Si nanoparticles in air and subsequent carbon coating and exhibit a reversible capacity of 786 mA h g^{-1} at a current density of 0.1 A g^{-1} after 100 cycles.[16] Ag@Si core-shell nanowall arrays were fabricated via the RF-sputtering deposition of Si on Ag nanowall arrays. As anode materials for LIBs, Ag@Si core-shell nanowall arrays maintained a discharge capacity of 1679 mA h g^{-1} at 2.1 A g^{-1} after 400 cycles.[17]

Cu is the beneficial element to improve the electrochemical performance of Si.[18] The copper coated Si nanowires fabricated by magnetron sputtering method showed a capacity retention of 2216 mA h g^{-1} at 2.1 A g^{-1} over 30 cycles.[19] Carbon wrapped Si and Cu_3Si composites were fabricated by in-situ polymerization with the presence of ballmilled Si and Cu powders. As anode materials, the composite showed 94 % capacity retention of the first charge capacity (518 mA h g^{-1}) over 20 cycles and presented much enhanced cycling stability compared with Si/C composites.[20] Carbon coated Si, Cu_3Si and Cu composites, synthesized by precipitation and pyrolysis method, showed the first capacity of 680 mA h g^{-1} and a retained capacity up to 87 % after 30 cycles.[21]

Herein, inspired by the catalytic mechanism of CuCl in Rochow reaction, described as reaction (1) and (2) for the reaction between CuCl and Si,[22,23] we synthesized Cu_3Si@Si core-shell nanoparticles by the solid-state reaction between CuCl and Si at 600 °C. It is proposed that the created nascent Cu in the reaction (1) could diffuse into Si and combine with Si to form Cu_3Si@Si core-shell structure as reaction (2) because of the high diffusion of Cu in Si at high temperature. [24]

$$4CuCl + nSi \rightarrow SiCl_4 + 4Cu^* + (n\text{-}1)Si \quad (1)$$

$$3Cu^* + (n\text{-}1)Si \rightarrow Cu_3Si + (n\text{-}2)Si \quad (2)$$

As anode materials for LIBs, Cu_3Si@Si core-shell nanoparticles deliver a reversible capacity of 1560.6 mA h g^{-1} at 1 A g^{-1} after 50 cycles, 903.6 mA h g^{-1} at 2 A g^{-1} over 400 cycles and an initial coulombic efficiency of 80.6 %, which are significantly higher than those of the raw Si nanoparticles. The enhanced electrochemical performance can be attributed to two aspects. Firstly, the conductivity of Cu_3Si@Si core-shell nanoparticles is improved with the formation of Cu_3Si, resulting in the higher columbic efficiency, lower electrochemical impedance and hence enhancing the electrochemical performance. For the other, Cu_3Si core function as a mechanical support can stabilize cycling performance.

X-ray powder diffractions (XRD) are utilized to determine the phases of the samples. Fig.1a presents the XRD pattern of the product obtained from reaction for 10 h after treated with slightly excess dilute HNO_3 (Sample-10 h-AT). All the reflection peaks in Fig. 1a can be indexed to a mixture of the cubic phase Si (labeled as "◆", JCPDS card, no. 27-1402) and the orthorhombic phase Cu_3Si (labeled as "▼", JCPDS card, no. 51-0916).[25] The content of Cu in Sample-10 h-AT is approximately 17.3 wt%, determined by X-ray fluorescence spectroscopy (XRF).

The nanostructure and morphology of Sample-10 h-AT derived from the solid-state reactions followed with the treatment of HNO_3 are characterized by transmission electron microscopy (TEM), as shown in Fig. 1. Fig. 1b exhibits the TEM image of Sample-10 h-AT, which reveals the typical core-shell morphology of the sample. Meantime, the boundary between Si and the core of Cu_3Si is also investigated by the high-resolution TEM (HRTEM). Fig. 1d, magnified from Fig. 1c shows two distinguishable fringes. From Fig. 1d, the d-spacing values of the lattice planes are 2.01 and 3.12 Å, which correspond well with that of (300) planes of the orthorhombic Cu_3Si crystals and (111) plane of the cubic Si crystals, respectively. Energy-dispersive X-ray (EDX) mapping analysis is also conducted to further investigate the elemental distribution of Si and Cu in the core-shell nanoparticles. The EDX mapping images of the Si and Cu element are presented in Fig. 1e-g, which show the distributions of Si and Cu element across the whole region. Notably, the distribution region of Cu element match well with the core region located in center field, which further proves the core-shell structure with Si capped Cu_3Si nanoparticles.

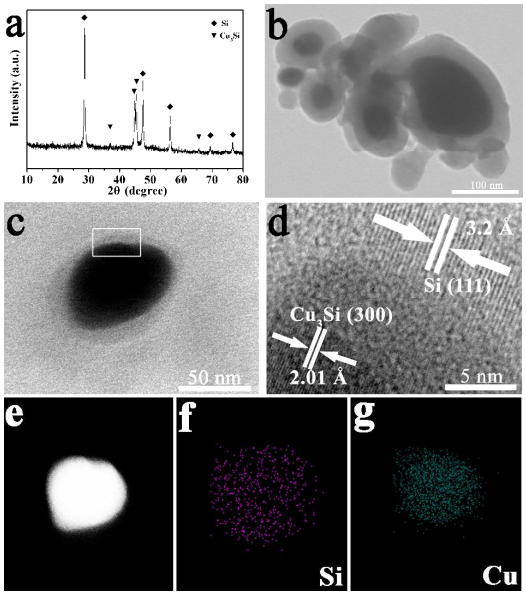

Fig. 1 XRD pattern (a) and the TEM images (b, c) of Sample-10 h-AT. (d) HRTEM image of highlighted by the rectangle in (c). (f–g) the corresponding EDX elemental mapping images of Si and Cu in the selected area (e).

Several time-dependent experiments were conducted to investigate the evolution process of Cu_3Si@Si nanoparticles with core-shell structure. As illustrated in Fig. 2a, the original Si nanoparticles show diameters below 200 nm. After the reaction proceeding 1 h, the corresponding products (Sample-1 h) consist of Si, Cu and Cu_3Si (XRD pattern in Fig. S1†), indicating that the reaction (1) and (2) started. TEM image (Fig. 2b) of Sample-1 h shows no core-shell structure. Meantime, the EDX mapping images (Fig. 2e-g) clearly disclose that part of Cu atoms came up on the surface of Si particles. After 6 h, the EDX mapping images (Fig. 2h-j) of the products (Sample-6 h) show that more Cu atoms have deeply diffused into the Si particles. TEM image of Sample-6 h (Fig. 2c) illustrates that a little part of core-shell structure has been created. However, there is some remained Cu according to the XRD pattern of Sample-6 h (Fig. S2a†). The remained Cu can be removed after the treatment of HNO_3, as identified by XRD pattern (Fig. S2b†). The TEM image (Fig. S3†) of Sample-6 h after treated with HNO_3 (Sample-6 h-AT) clearly shows a part of hollow structures, which are formed by the dissolved Cu and exposed Cu_3Si alloy. When 10 h was applied, the typical core-shell structure was obtained (Fig. 2d). Meanwhile, there is also some excessive Cu in Sample-10 h according to XRD patterns (Fig. S4† and Fig. 1a), which can be removed by dilute HNO_3. At the same time, the core-shell structures can be kept after the treatment of dilute HNO_3. When reaction prolonged to 20 h, Cu_3Si@Si core-shell strucutre (Sample-20 h-AT, XRD and TEM image showed in Fig. S5†) was still persevered after treated with HNO_3. Examined by XRF, the Cu content in Sample-20 h-AT was 17.1 w%, which was almost the same with that of Sample-10 h-AT, indicating that nearly no change happened after 10 h.

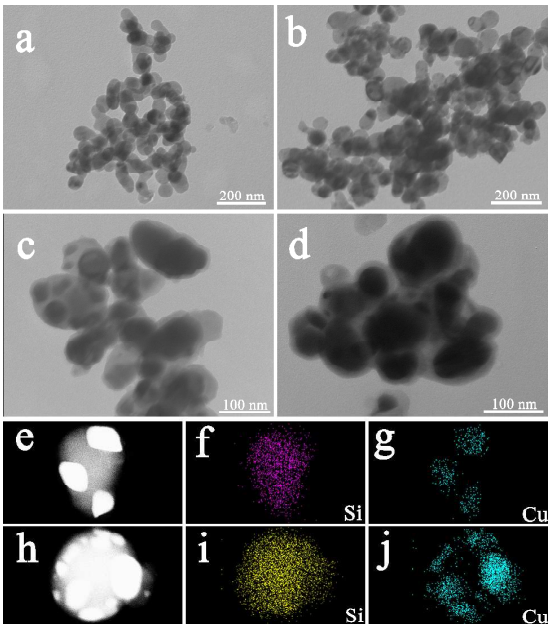

Fig. 2 TEM images of Cu_3Si@Si core-shell nanoparticles from the reaction of CuCl and Si at different reaction time before treated with dilute HNO_3: (a) 0 h, (b) 1 h, (c) 6 h, (d) 10 h. The element mapping images of Sample-1 h (e-g) and Sample-6 h (h-j).

Because Cu has a higher diffusion coefficient in Si than that of Si in Cu, Cu atoms would diffuse into Si particles at high temperature.[24,26] Since the solid state reaction between CuCl and Si would start on the surface of Si, the diffusion of Cu in Si from surface is kinetically slow. In our experiment, with the time and reaction going on, Cu atoms can further diffuse into Si and merge in the core for the formation of Cu_3Si alloy at 600 °C. When time comes to 10 h, nearly no change can be observed after that, which indicate an evolution mechanism analogous to Kirkendall effect.[27,28], Therefore, the formation of Cu_3Si core in Si is on the

basis of time dependent Kirkendall effect. Meanwhile, based on the calculation of free energy, equation (1) is thermodynamically spontaneous and exothermic ($\Delta_r G_m$= -165.87 kJ mol^{-1}, $\Delta_r H_m$= -170.75 kJ mol^{-1}). The released large amount of heat and the nascent Cu can further promote the formation of Cu_3Si@Si core-shell structure. In order to prove that, contrast experiments were conducted. Cu powder and Si powder were mixed with the corresponding ratio and treated under the same condition for 10 h. However, no Cu_3Si can be detected by XRD (Fig. S6†) and no core-shell structure can be observed in TEM image (Fig. S7†).

The electrochemical properties of Si, Sample-6 h-AT and Sample-10 h-AT anodes are investigated with lithium foil as a counter in CR2016-type coin cell. Fig. 3a exhibits the typical cyclic voltammetry (CV) curves of Cu_3Si@Si core-shell nanoparticles from 1st to 5th cycle at a scanning rate of 0.1 mV s^{-1} in the potential window of 0.01-1.5 V vs. Li/Li$^+$. In the cathodic part of first cycle, an inconspicuous peak located around 1.14 V, disappearing in the following cycles, can be attributed to the formation of SEI membrane, which leads to the irreversible capacity in the initial cycle.[29] At the same time, the sharp peak below 0.1 V appearing in the 1st cycle represents the alloy reaction of crystallized Si and Li$^+$. In the subsequent cycles, the peak below 0.1 V is replaced by the peak at 0.18 V due to the amorphization of crystalline Si after the initial process of lithiation.[30] The predominant peaks at 0.34 V and 0.53 V from 1st to 5th cycle in the anodic part represent the lithium extraction potential, which can be assigned to the reaction between Li and Si and the formation of amorphous Si.[31] It's notable that the CV curves of Sample-10 h-AT anode show no difference from these of commercial Si anode (Fig. S8†), because Cu is the inactive material for LIBs, which cannot react with Li$^+$.[20]

Fig. 3b shows the first cycle's voltage versus capacity profiles of three electrodes at the current density of 0.2 A g^{-1} with the voltage window of 0.01-1.5 V. It is evident that the discharge process of the three samples with an accordant voltage plateau of about 0.1 V (vs. Li/Li$^+$) manifests typical characteristics of Si voltage trends and agrees well with the lithiation process of crystallized Si.[32] In the examined range, the first discharge capacity of Si, Sample-6 h-AT and Sample-10 h-AT is 3948.3, 3284.6 and 2805.8 mA h g^{-1} and the charge capacity is 2571.4, 2364.1 and 2260.2 mA h g^{-1} with the corresponding initial coulombic efficiency of 65.1, 71.9 and 80.6 %, respectively. The irreversible capacity is caused by the formation of SEI membrane and the irreversible intercalation of Li$^+$ in Si.[33] The improved

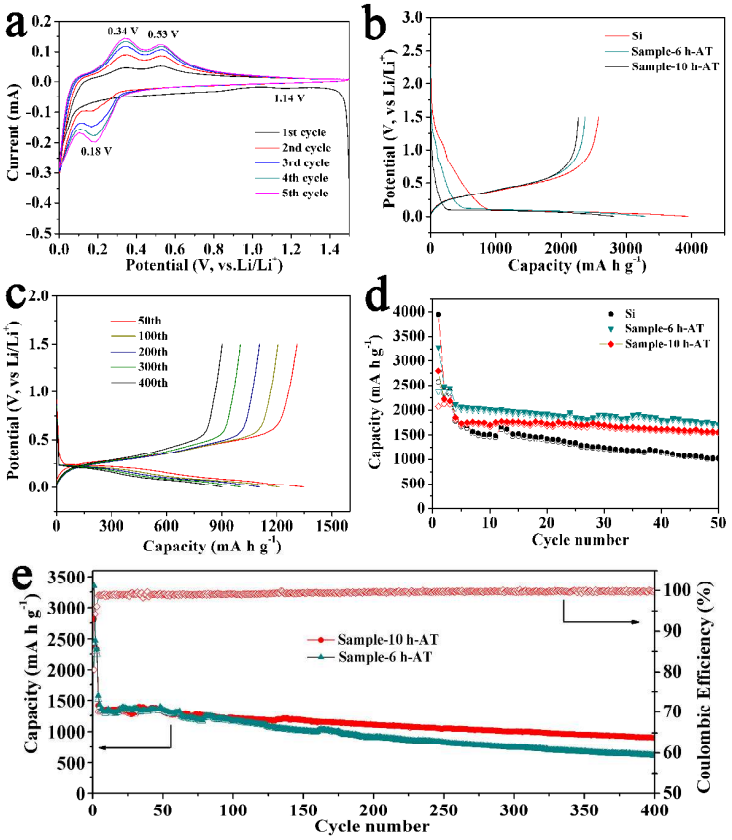

Fig. 3 (a) Cyclic voltammetry curves of the Sample-10 h-AT electrode of 1st-5th cycles. (b) Initial discharge/charge voltage profiles of Si, Sample-6 h-AT and Sample-10 h-AT at a current density of 0.2 A g^{-1}. (c) Discharge/charge voltage profiles for Sample-10 h-AT of 50th, 100th, 200th, 300th and 400th cycles at 2 A g^{-1}.(d) Cycling performance of Si, Sample-6 h-AT and Sample-10 h-AT anodes at 1 A g^{-1}. (d) Cycling performance and the coulombic efficiency of Sample-6 h-AT and Sample-10 h-AT anodes at 2 A g^{-1}. Notably, the first three cycles of all the cells are tested at a relatively low current density of 0.2 A g^{-1} to sufficiently activate anode materials.

initial coulombic efficiency of Sample-6 h-AT and Sample-10 h-AT comparing with Si is associated with the added Cu in the core,which can enhance the conductivity of electrodes.[34]

Fig. 3c reveals the discharge/charge curves of Sample-10 h-AT in the 50th, 100th, 200th, 300th and 400th cycles with a current density of 2 A g^{-1}. The discharge potential plateau curves, around 0.1 V (vs. Li/Li^+) that showed in the Fig. 3b, are replaced by a group of sloping curves that result from the amorphization of Si after the first lithiation/delithiation. In addition, the potential plateau curves from 50th and 400th are superimposed well, indicating good reversible electrochemical reaction between Li^+ and Sample-10 h-AT electrode.

Furthermore, the cycling behavior of Si, Sample-6 h-AT and Sample-10 h-AT electrodes are evaluated at two different current densities by galvanostatic measurements. Fig. 3d comparatively describes the cycling performance of the three electrodes at a current of 1 A g^{-1}. Notably, in order to activate Si nanoparticles sufficiently, the first three cycles of all the cells are tested at a relatively low current density of 0.2 A g^{-1}. After 50 cycles, Si, Sample-6 h-AT and Sample-10 h-AT electrodes retain a discharge capacity of 1024.6, 1715.3 and 1560.6 mA h g^{-1}, respectively. Despite the decay of capacity in the first three cycles caused by the formation of SEI membrane, 55.6, 81.5 and 89.2 % capacity retention are obtained for Si, Sample-6 h-AT and Sample-10 h-AT electrodes over 50 cycles, corresponding to the average capacity fading rate of 0.89, 0.37 and 0.23 % per cycle, respectively. Even though Sample-6 h-AT shows the highest capacity retention at 1 A g^{-1} after 50 cycles, Sample-10 h-AT exhibits a more stable cycling performance than that of Sample-6 h-AT and Si. The long term cycling performance of Sample-6 h-AT and Sample-10 h-AT at a high current density is also studied (showed in Fig. 3e). As shown, when the current density increases to 2 A g^{-1}, Sample-10 h-AT anode delivers a specific capacity of 903.6 mA h g^{-1} over 400 cycles, which is much higher than that of Sample-6 h-AT anode with 609.6 mA h g^{-1}. The corresponding coulombic efficiency curve of Sample-10 h-AT (Fig. 3e) quickly increases from 81 % of first cycle to 96.5 % of the second cycle and further reaches over 97 % after several cycles. The cycling performance at high current density indicates the good rate performance of Sample-10 h-AT.

The good electrochemical performance of Sample-10 h-AT can be ascribed to the following aspects. Firstly, the nano-sized Sample-10 h-AT particles can easily relax the strain experienced from the repeated discharge and charge process and keep the mechanical integrity, and facilitate the transmission of ionic and electronic in short distance.[33,35] More importantly, the conductivity of Sample-10 h-AT is further improved with the addition of Cu, which results in a higher columbic efficiency, lower electrochemical impedance and enhanced electrochemical performance. The superior electron conductivity of Sample-10 h-AT is confirmed by the distinctly reduced diameter of the semicircle at high-to-medium frequency region in the electrochemical impedance spectroscopy (Fig. S9†). At the same time, Cu_3Si, as the core of Cu_3Si@Si nanoparticles, can function as the mechanical support, stabilize the structure and lead to a stabilized cycling performance.[17] Fig. S10 shows the maintained core-shell structure of Sample-10 h-AT after 400 cycles at 2 A g^{-1}.

Conclusions

In summary, Cu_3Si@Si core-shell nanoparticles are synthesized by a simple solid-state reaction. The evolution process of Cu_3Si@Si nanoparticles with core-shell structure is examined by a series of time-dependent experiments, which indicate an evolution mechanism analogous to Kirkendall effect. When evaluated as anode materials for lithium ion batteries, Cu_3Si@Si core-shell nanoparticles exhibit good cycling stability and rate performance and deliver a reversible capacity of 1560.6 mA h g^{-1} at 1 A g^{-1} after 50 cycles, and 903.6 mA h g^{-1} at 2 A g^{-1} over 400 cycles. The enhanced electrochemical performance can be attributed to the enhanced conductivity and the core-shell structure.

Acknowledgments

The authors would like to appreciate the financial support from the 973 Project of China (No. 2011CB935901), the National Natural Science Fund of China (No. 91022033, 21201158), and the Specialized Research Fund for the Doctoral Program of Higher Education (No. 20133402110047).

Notes and references

[a] *Hefei National Laboratory for Physical Science at Microscale, University of Science and Technology of China, Hefei, 230026, P.R. China. Tel: +86-551-63601589; E-mail: ychzhu@ustc.edu.cn; ytqian@ustc.edu.cn.*

† Electronic Supplementary Information (ESI) available. See DOI: 10.1039/b000000x/

1. B. A. Boukamp, G. C. Lesh and R. A. Huggins. *J. Electrochem. Soc.*, 1981, **128**, 725.
2. M. Y. Ge, J. P. Rong, X. Fang and C. W. Zhou, *Nano Lett.*, 2012, **12**, 2318.
3. L. B. Wang, N. Lin, J. B. Zhou, Y. C. Zhu, and Y. T Qian, *Chem. Commun.*, 2015, **51**, 2345.
4. C. K. Chan, H. L. Peng, G. Liu, K. McIlwrath, X. F. Zhang, R. A. Huggins and Y Cui, *Nat. Nanotechnol.*, 2008, **3**, 31.
5. B. M. Bang, J. I. Lee, H. Kim, J. Cho and S. Park, *Adv. Energy Mater.*, 2012, **2**, 878.
6. S. H. Ng, J. Z. Wang, D. Wexler, K. Konstantinov, Z. P. Guo and H. K. Liu, *Angew. Chem. Int. Edit.*, 2006, **45**, 6896.
7. Y. Yu, L. Gu, C. Zhu, S. Tsukimoto, P. A. Van aken and J. Maier, *Adv. Mater.*, 2010, **22**, 2247.
8. I. S. Kim, P. N. Kumta and G. E. Blomgren, *Electrochem. Solid St.*, 2000, **3**, 493.
9. M. T. McDowel, S. W. Lee, C. M. Wang and Y. Cui, *Nano Energy*, 2012, **1**, 401.

10. M. Thakur, R. B. Pernites, N. Nitta, M. Isaacson, S. L. Sinsabaugh, M. S. Wong and S. L. Biswa, *Chem. Mater.*, 2012, **24**, 2998.
11. J. Chang, X. Huang, G. H. Zhou, S. Cui, P. B. Hallac, J. W. Jiang, P. T. Hurley and J. H. Chen, *Adv. Mater.*, 2013, **26**, 758.
12. B. Wang, X. Li, X. Zhang, B. Luo, M. Jin, M. Liang, S. A. Dayeh, S. T. Picraux and L. J. Zhi, *ACS Nano*, 2013, **7**, 1437.
13. N. Lin, J. B. Zhou, Y. C. Zhu and Y. T Qian, *J. Mater. Chem. A*, 2014, **2**, 19604.
14. P. F. Gao, J. W. Fu, J. Yang, R. G. Lv, J. L. Wang, Y. N. Nuli and X. Z. Tang, *Phys. Chem. Chem. Phys.*, 2009, **11**, 11101.
15. Z. Sun, X. F. Song, P. Zhang and L. Gao, *RSC Adv.*, 2014, **4**, 20814.
16. H. C. Tao, X. L. Yang, L. L. Zhang and S. B. Ni, *Ionics*, 2014, **20**, 1547.
17. W. J. Zhao, N. Du, C. M. Xiao, H. Wu, H. Zhang and D. R. Yang, *J. Mater. Chem. A*, 2014, **2**, 13949.
18. V. A. Sethuraman, K. Kowolik and V. Srinivasan, *J. Power Sources*, 2011, **196**, 393.
19. H. X. Chen, Y. Xiao, L. Wang and Y. Yang, *J. Power Sources*, 2011, **196**, 6657.
20. K. Wang, X. M. He, L. Wang, J. G. Ren, C. Y. Jiang and C. R. Wan, *Solid State Ionics*, 2007, **178**, 115.
21. J. H. Kim, H. Kim and H. Sohn, *J. Electrochem. Commun.*, 2005, **7**, 557.
22. E. G. Rochow, *J. Am. Chem. Soc.*, 1945, **67**, 963.
23. J. Acker, S. Köther, K. M. Lewis and K. Bohmhammel, *Silicon Chemistry*, 2003, **2**, 195.
24. A. A. Istratov and E. R. Weber, *J. Electrochem. Soc.*, 2002, **149**, 21.
25. S. Yoon, S. Lee, H. Kim and H. J. Sohn, *J. Power Sources*, 2006, **161**, 1319.
26. C. H. Chiu, C. W. Huang, J. Y. Chen, Y. T. Huang, J. C. Hu, L. T. Chen, C. L. Hsin and W. W. Wu, *Nanoscale*, 2013, **5**, 5086.
27. Y. He, Y. H. Wang, X. Q. Yu, H. Li and X. J. Huang, *J. Electrochem. Soc.*, 2012, **159**, 2076.
28. J. Lee, J. C. Park and H. Song, *Adv. Mater.*, 2008, **20**, 1523.
29. S. E. Lee, H. J. Kim, J. H. Park and D. Choi, *Nanoscale*, 2013, **5**, 8986.
30. E. Radvanyi, E. D. Vito, W. Porcher, J. Danet, P. Desbois, J. F. Colin and S. J. Larbia, *J. Mater. Chem. A*, 2013, **1**, 4956.
31. M. Gauthier, D. Mazouzi, D. Reyter, B. Lestriez, P. Moreau and D. Guyomard, *Energy Environ. Sci.*, 2013, **6**, 2145.
32. Y. H. Zhu, W. Liu, X. Y. Zhang, J. C. He, J. T. Chen, Y. P. Wang and T. B. Cao, *Langmuir*, 2013, **29**, 744.
33. H. Wu, G. Chan, J. W. Choi, I. Ryu, Y. Yao, M. T. McDowell, S. W. Lee, A. Jackson, Y. Yang, L. B. Hu and Y. Cui, *Nat. Nanotechnol.*, 2012, **7**, 310.
34. C. H. Chiu, C. W. Huang, J. Y. Chen, Y. T. Huang, J. C. Hu, L. T. Chen, C. L. Hsin and W. W. Wu, *Nanoscale*, 2013, **5**, 5086.
35. J. R. Szczech and S. Jin, *Energy Environ. Sci.*, 2011, **4**, 56.